



Cite this: *RSC Adv.*, 2022, 12, 21145

# The solvent-free mechano-chemical grinding of a bifunctional P25–graphene oxide adsorbent–photocatalyst and its configuration as porous beads†

Fatima-Ezzahra Zrar,<sup>ab</sup> Nadia Katir,<sup>a</sup> Samir Qourzal,<sup>b</sup> Ihya Ait Ichou<sup>b</sup> and Abdelkrim El Kadib <sup>\*a</sup>

Owing to their use in water-cleaning technology, titanium-dioxide-based nanomaterials have dominated the photocatalysis scene, with so-called Degussa (P25) being the most promising under UV light. However, this is not the case under visible light, where it is necessary to combine titanium dioxide with other photosensitising nanomaterials. Unfortunately, most of the strategies aimed in this direction are chemically non-facile, energy-intensive, economically expensive, and not suitable for large-scale production. We herein describe a straightforward solvent-free approach for accessing visible-light-activated titanium-dioxide-based photocatalysts *via* the mechanochemical grinding of Degussa P25 with a second solid partner. Upon comparing several solid-material benchmarks, P25–graphene oxide is the best combination. The resulting material showed efficient performance for the adsorption and photodegradation of different dye pollutants, namely methylene blue, malachite green, Congo red, and methyl orange. The recorded performance was nearly comparable to that reached using sol–gel materials, with the ultimate advantage of being more sustainable and industrially scalable. The recyclability can be improved through a porous-bead configuration using biomass waste chitosan hydrogel, an approach that can further fulfill the requirement for more sustainable photocatalyst designs.

Received 29th June 2022  
Accepted 15th July 2022

DOI: 10.1039/d2ra04017d

rsc.li/rsc-advances

## Introduction

First discovered in 1972, titanium dioxide is the most famous photocatalyst to date,<sup>1</sup> and it is expected to be a key player in sewage treatment and water-cleaning technology worldwide.<sup>2</sup> While many titanium dioxide ceramics are industrially available, with so-called Degussa P25 being the most ubiquitous,<sup>3</sup> they still have many limitations, including low surface areas, poor activities under visible light, and moderate photo-stability and electron–hole recombination properties.<sup>4</sup> With the emergence of nanostructured hybrid materials, efforts have focused on exploring wet chemistry to closely combine titanium dioxide with other nanostructures, starting from soluble precursors.<sup>5</sup> Substantial knowledge has been gleaned from these approaches, enabling researchers to circumvent most of the bottlenecks associated with titanium dioxide *via* increasing the specific surface area, improving the framework crystallinity,

and expanding the working region to the most suitable visible-light region instead of the constraining UV region.<sup>6</sup> Although there is a broad range of reported titanium-dioxide-based photocatalysts,<sup>7</sup> most of them are prepared through non-facile and energy-intensive procedures, consequently generating little allure for large-scale production.<sup>8</sup>

A popular current trend consists of the development of bifunctional adsorbent–photocatalyst nanocomposites *via* merging two or more components.<sup>8,9</sup> Illustrative examples include the association of high-surface-area materials and inorganic semiconductors,<sup>10</sup> and the creation of heterojunctions *via* closely combining two different photoactive materials, resulting in tuneable visible-light photoactivity.<sup>11</sup> In this context, conductive graphitic carbon materials have shown efficiency as photosensitizing partners,<sup>12</sup> with many precedents in the literature demonstrating the combination of titanium dioxide (including P25) with both graphene oxide (GO) and carbon nanotubes (CNTs).<sup>13</sup>

Given the prominence of the target applications, with specific consideration given to the urgent issues of sustainable energy generation and water management,<sup>14</sup> it is highly recommended to set up straightforward, scalable, and cost-effective methods to transform already available ceramics into highly active visible-light photocatalysts.<sup>12b,15</sup>

<sup>a</sup>*Euromed Research Center, Engineering Division, Euro-Med University of Fes (UEMF), Route de Meknes, Rond-Point de Bensouda, 30070, Fès, Morocco. E-mail: a.elkadib@ueuromed.org*

<sup>b</sup>*Materials, Photocatalysis and Environment Team, Department of Chemistry, Faculty of Sciences, Ibn Zohr University, B. P. 8106, Dakhla City, Agadir, Morocco*

† Electronic supplementary information (ESI) available. See <https://doi.org/10.1039/d2ra04017d>



We herein report that the minute grinding of biphasic anatase-rutile  $\text{TiO}_2$  (P25) in the presence of graphene oxide (GO) affords an active visible-light photocatalyst for dye degradation in water. Exhaustive screening reveals that  $\text{TiO}_2$ @GO is the most attractive combination, outperforming a set of other attractive nanomaterials, including graphite, carbon nanotubes, active carbon, boron nitride, layered montmorillonite, and tubular halloysite. The resulting powdered material could also be configured using seafood waste chitosan, which is known to provide hydrogels. Our results bring evidence for the suitability of this configuration approach to further improve the recyclability of the as-prepared photocatalyst, which opens up more possibilities for tackling the thorny issue of the long-term use of catalysts under continuous-flow conditions.

## Results and discussion

We first screened a large variety of mechanochemically ground powder samples based on the combination of titanium dioxide with carbon materials, clay, and boron nitride. In the carbon-based series, we used graphite (G), graphene oxide (GO), phosphorylated graphene (PGO), carbon nanotubes (CNTs), carbon nitride ( $\text{C}_3\text{N}_4$ ), and activated carbon (AC) as grindable partners for Degussa P25. We also selected both montmorillonite (MMT) and halloysite (HNT) as representative clay materials, owing to their interesting lamellar and tubular topologies, respectively.<sup>16</sup> We moreover assessed the mechanochemical mixing of titanium dioxide with lamellar boron nitride owing to the promising properties of the latter.<sup>17</sup> For these combinations, the same ratio (45 wt%  $\text{TiO}_2$  and 55 wt% second phase) was used. The materials were denoted as  $\text{TiO}_2$ @X-45 : 55, with X referring to the second phase, while 45 and 55 indicate the weight percentages of  $\text{TiO}_2$  and X, respectively.

After grinding and further homogenisation, the resulting solids were used for the photodegradation of methylene blue as a representative textile dye pollutant. The photocatalytic results presented in Fig. 1 show the methylene blue degradation

kinetics and the overall performance, combining both adsorption and photodegradation.

Obviously, the most active combination is  $\text{TiO}_2$ @GO-45 : 55, allowing 82% of the dye to be removed. The performance is very high; the second most active material,  $\text{TiO}_2$ @AC-45 : 55, did not exceed 51%.  $\text{TiO}_2$ @G-45 : 55 displayed poor photoactivity, enabling the degradation of only 12% of the dye. Although clay-based materials are well-known adsorbents, their performance levels (43% for  $\text{TiO}_2$ @MMT-45 : 55 and 29% for tubular  $\text{TiO}_2$ @HNT-45 : 55) remain far from that reached using  $\text{TiO}_2$ @GO-45 : 55. Interestingly,  $\text{TiO}_2$ @GO-45 : 55 works efficiently as both an adsorbent and photocatalyst, suggesting that both titanium dioxide and graphene oxide provide activity, probably in a synergistic manner. The high adsorption of methylene blue by graphene oxide has been reported in the literature, and it has been attributed to favourable  $\pi$ - $\pi$  stacking interactions.<sup>18</sup> Adsorption on MMT commonly occurs through cation exchange with sodium located inside of the material galleries;<sup>19</sup> in the case of HNT, hosting occurs *via* the diffusion of the pollutant inside of the lumen.<sup>20</sup> The poor performance recorded with graphite was surprising given the similarities of its molecular structure to that of graphene oxide. However, in graphite, the sheets are stacked in a layered fashion, making the diffusion of pollutants difficult. In turn, as will be discussed below, graphene oxide seems to be already exposed through sheet exfoliation induced upon mechanical grinding with titanium dioxide particles.<sup>21</sup>

Having demonstrated the superiority of  $\text{TiO}_2$ @GO with respect to its competitors, we next investigated the effects of the weight ratio ( $\text{TiO}_2$ @GO) on the final performance. For this purpose, we used three different materials, namely  $\text{TiO}_2$ @GO-45 : 55,  $\text{TiO}_2$ @GO-05 : 95, and  $\text{TiO}_2$ @GO-95 : 05. These materials have different compositions; one is enriched with graphene oxide phase, one is enriched with titanium dioxide, and one has a good balance between the two phases.

The three materials were next characterized using X-ray diffraction (XRD), Raman spectroscopy, nitrogen sorption, and scanning electron microscopy (SEM) analyses (Fig. 2 and 3). The XRD patterns of these materials display the fingerprint of

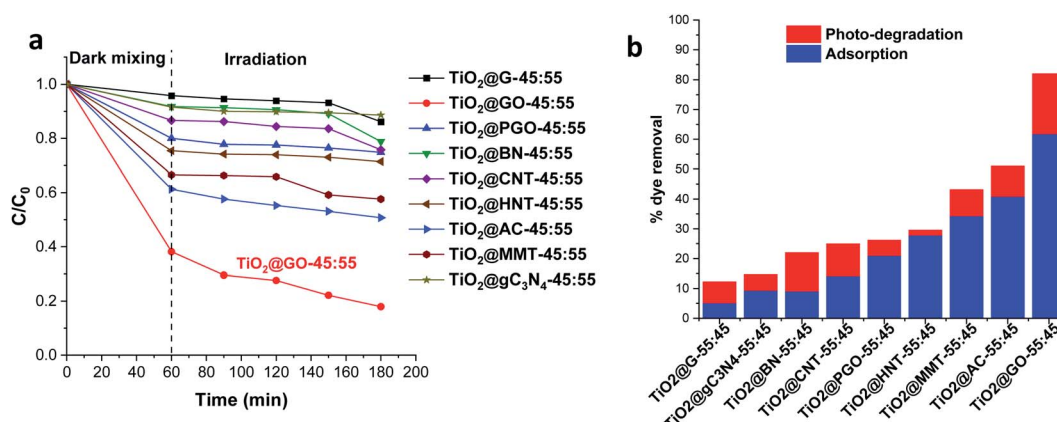


Fig. 1 Methylene blue degradation using a set of hybrid materials built from the mechanochemical grinding of P25 Degussa with a second phase: (a) the degradation kinetics and (b) the amount of removed dye (%), combining adsorption and photocatalysis.



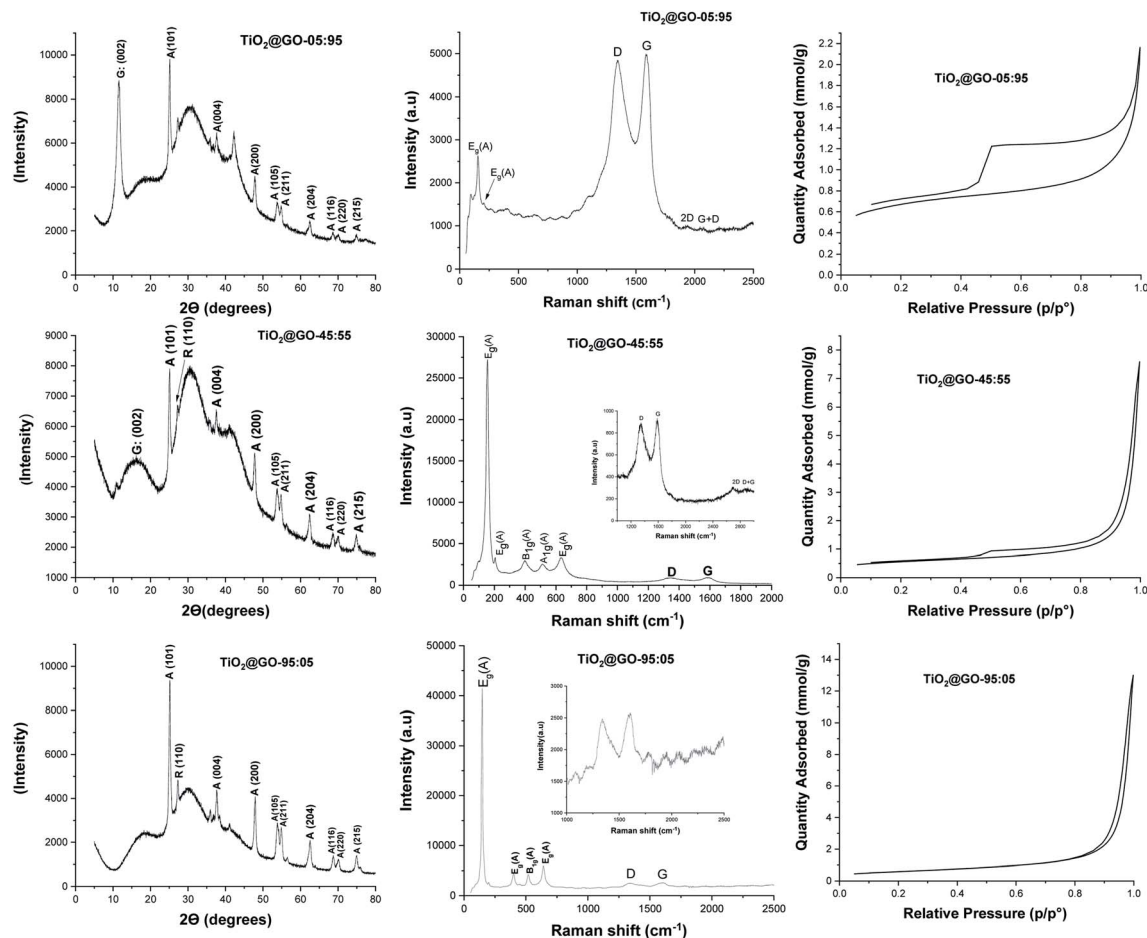


Fig. 2 (Left column) XRD spectra, (middle column) Raman spectra, and (right column) nitrogen adsorption–desorption isotherms of the mechanically ground materials: top,  $\text{TiO}_2\text{:GO-05 : 95}$ ; middle,  $\text{TiO}_2\text{:GO-45 : 55}$ ; bottom,  $\text{TiO}_2\text{:GO-95 : 05}$ .

Degussa with no significant shifts or variations upon mixing with GO. Both anatase and rutile peaks are identified. In addition, a single peak assignable to the 002 plane of graphene oxide at  $2\theta = 10^\circ$  could be observed for  $\text{TiO}_2\text{:GO-95 : 05}$ , while it was barely visible for  $\text{TiO}_2\text{:GO-45 : 55}$  and invisible for  $\text{TiO}_2\text{:GO-95 : 05}$ . The decrease and disappearance of this signal could be attributed to the exfoliation of sheets during grinding, which becomes more significant upon increasing the amount of titanium dioxide.

Raman spectroscopy reveals the typical pattern of the graphitic phase, with the two characteristic D and G bands in

the ranges of  $\sim 1341$  to  $1349\text{ cm}^{-1}$  and  $\sim 1588$  to  $1604\text{ cm}^{-1}$ , respectively.<sup>22</sup> The  $I_D/I_G$  ratio was found to be 0.96 for the material with the lowest amount of graphene oxide, 0.96 for the medium-level material, and 0.97 for the material enriched with graphene oxide. The intensities of the carbon-zone peaks *versus* the titanium-dioxide-zone peaks vary consistently with the GO :  $\text{TiO}_2$  ratio; two intense carbon signals are observed for  $\text{TiO}_2\text{:GO-05 : 95}$  while more crystalline peaks of titanium dioxide are observed for  $\text{TiO}_2\text{:GO-95 : 05}$  and  $\text{TiO}_2\text{:GO-45 : 55}$ . Nitrogen sorption analysis shows nearly the same specific surface area for all materials ( $47\text{ m}^2\text{ g}^{-1}$ ,  $41\text{ m}^2\text{ g}^{-1}$ , and

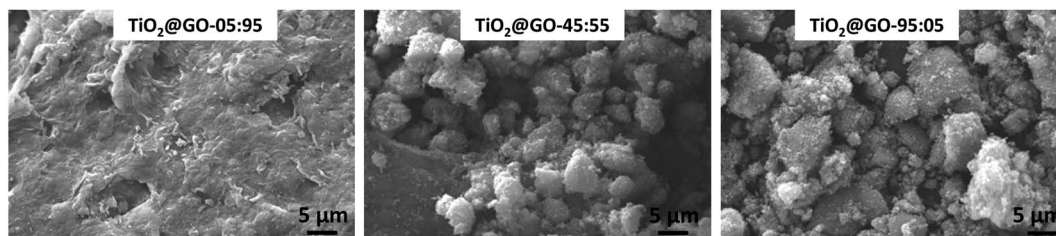


Fig. 3 Scanning electron microscopy (SEM) images of the prepared materials: from left to right,  $\text{TiO}_2\text{:GO-05 : 95}$ ;  $\text{TiO}_2\text{:GO-45 : 55}$ ; and  $\text{TiO}_2\text{:GO-95 : 05}$ .

48 m<sup>2</sup> g<sup>-1</sup> for TiO<sub>2</sub>@GO-95 : 05, TiO<sub>2</sub>@GO-45 : 55, and TiO<sub>2</sub>@GO-05 : 95, respectively). Although no significant variations in specific surface area could be observed, the isotherm profiles are quite different for the three materials, mainly in the case of TiO<sub>2</sub>@GO-05 : 95, which shows the pronounced development of hysteresis and an increase in total microporosity. This situation could be triggered by the dominance of the graphitic network and the presence of tactoids and small voids at the interface of carbon and the ceramic phase. In turn, the TiO<sub>2</sub>@GO-45 : 55 network seems to be made of large mesopores that extend to the macroporous domain as a consequence of sheet exfoliation due to titanium dioxide. Porosity seems to be brought about by titanium dioxide particles and the internal voids created by their entanglement with graphitic sheets.

SEM analyses allow for the visualisation of the networks on the microscale (Fig. 3 and S1†). Nicely, the morphology of the network depends on the predominant phase. For TiO<sub>2</sub>@GO-05 : 95, the typical network of graphene oxide is observed, with a few spherical P25 particles embedded. In TiO<sub>2</sub>@GO-45 : 55, agglomerated particles of titanium dioxide appear along with the flat layers of graphene oxide. In TiO<sub>2</sub>@GO-95 : 05, graphenic sheets could hardly be detected in a network that was dominated by the presence of aggregated titanium dioxide particles (Fig. 3).

It is consequently reasonable to attribute the behaviour of each material to the dominant phase. We next investigated the photocatalytic activities of the three materials toward different representative dye contaminants, including methylene blue, green malachite, Congo red, and methyl orange. The results are gathered in Fig. 4 and the kinetics are shown in the ESI (Fig. S2†). The order of performance seems to be dependent on the loading of graphene oxide. The highest photooxidation activity was observed at high graphene loading (TiO<sub>2</sub>@GO-05 : 95), followed by TiO<sub>2</sub>@GO-45 : 55 and then TiO<sub>2</sub>@GO-95 : 05.

This trend is expected for photocatalysis under visible light, as P25 Degussa do not display any appreciable activity.<sup>23</sup> In turn, graphene oxide brings additional adsorption sites<sup>18</sup> and also acts as a photosensitizer for titanium dioxide.<sup>24</sup> Within the dye series, the degradation of methylene blue and malachite green seems to be more quantitative (~90% degradation reached with TiO<sub>2</sub>@GO-05 : 95). In contrast, methyl orange and Congo red

are more difficult to degrade during the advanced oxidation process, as illustrated by the moderate amount of removed dye, which remains at less than 32%. Overall, the utility of mixing titanium dioxide with graphene is evident when comparing the overall performances of the hybrids with that of native Degussa P25 titanium dioxide (Fig. S3†).

Attempts to further improve the experimental protocol do not boost the catalytic performance. For instance, subjecting the mixture to sonication and wetting with ethanol (TiO<sub>2</sub>@GO<sub>us</sub>, us refers to ultrasonication) failed to further improve the performance. Refluxing in boiling ethanol also did not improve the performance (TiO<sub>2</sub>@GO<sub>reflux</sub>) (Fig. 5a). This indicates that close contact was already obtained during the solvent-free mechano-chemical grinding of the two phases, with the possible exfoliation of GO sheets suspected to be the driving force behind such tight interplay.<sup>21</sup>

The accessibility of the titanium dioxide phase *versus* the graphene phase should also be taken into account during photooxidation. We have consequently compared the mechanically ground material to TiO<sub>2</sub>@GO<sub>sol-gel</sub> and TiO<sub>2</sub>@CS<sub>pyr</sub>. The first material was prepared through the post-grafting of titanium alkoxide onto graphene oxide<sup>22</sup> followed by thermal annealing treatment to generate crystalline titanium dioxide grown on the external surface of graphene.<sup>23</sup> The second photocatalyst was prepared *via* mixing chitosan and titanium alkoxide in a sol-gel process followed by carbonization under nitrogen to generate well-entangled titanium dioxide inside of the carbonaceous graphene network (see the Experimental section for details and Fig. S4† for more characterization data). In this case, chitosan serves as the carbon source<sup>25</sup> and as a structure-directing agent for titanium alkoxide mineralization.<sup>26</sup>

Comparing the photoactivities of the three materials shows that TiO<sub>2</sub>@GO-45 : 55 displays interesting photoactivity, quite comparable to TiO<sub>2</sub>@GO<sub>sol-gel</sub>. In turn, very moderate activity was revealed for TiO<sub>2</sub>@CS<sub>pyr</sub>, mainly during irradiation. This poor photoactivity can be correlated with the restricted exposure of titanium dioxide particles that are sequestered inside of the generated carbon network. The poor graphitisation of the network leaves abundant amorphous regions that can further worsen the photoactivity of the resulting material, as a temperature above 900 °C under argon is often claimed to be necessary

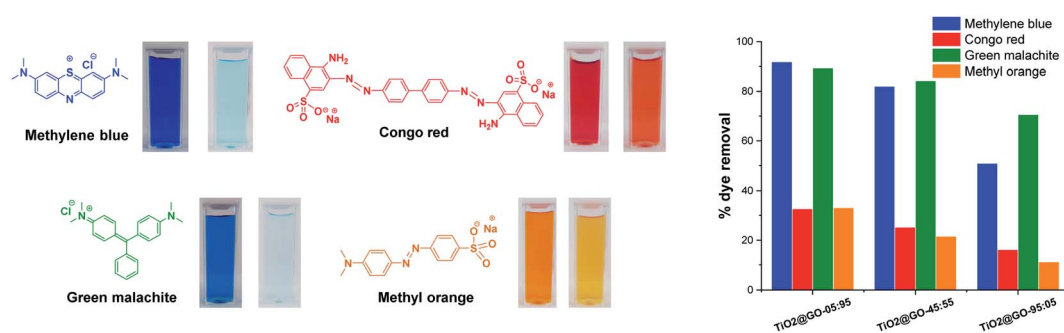


Fig. 4 A schematic representation of the four dye contaminants investigated in this work with photos showing the colors before and after photo-treatment. The panel on the right illustrates the removal efficiencies recorded for the three materials.





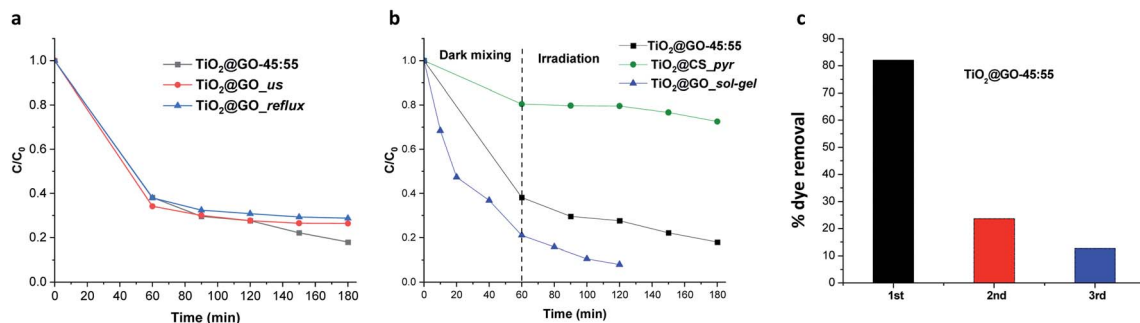


Fig. 5 (a) The photocatalytic activity of  $\text{TiO}_2@\text{GO}$  depending on the experimental procedure. (b) The photocatalytic activity of the ground material *versus* sol-gel and carbonized analogues. In these materials, the accessibility to titanium dioxide particles diverges substantially, making a comparison useful for probing the effects of photocatalyst exposure. (c) Recycling experiments with the ground powder, showing the fast deactivation.

to generate a uniform graphitised carbon network from chitosan polymer.<sup>27</sup> The slight increase in the activity of  $\text{TiO}_2@\text{GO}_{\text{sol-gel}}$  could be attributed to (i) more exposed titanium dioxide particles, (ii) favourable interfacial contact between the ceramic and the carbon phase through covalent bonding, and (iii) improved graphene quality due to the removal of oxygenated groups on the surface during thermal annealing treatment. The outstanding adsorptive capacity of  $\text{TiO}_2@\text{GO}_{\text{sol-gel}}$  with respect to  $\text{TiO}_2@\text{GO-45 : 55}$  can be explained based on differences in their specific surface areas, as estimated by nitrogen sorption; the former has a value of  $186 \text{ m}^2 \text{ g}^{-1}$ , while a value of only  $41 \text{ m}^2 \text{ g}^{-1}$  was recorded for the mechanically ground material. Although interesting, it is worth mentioning that  $\text{TiO}_2@\text{GO}_{\text{sol-gel}}$  was prepared through a multistep procedure<sup>22</sup> involving expensive precursors and calcination at high temperature,<sup>23</sup> while a very trivial mechanical grinding procedure was applied in the case of  $\text{TiO}_2@\text{GO-45 : 55}$  (Fig. 5b).

Recycling experiments show the main limitations of the ground material, as fast deactivation was noticed during the second cycle, and the photoactivity almost completely vanished after further use (Fig. 5c).

We have decided to assess the photostability of these materials under similar reaction conditions. Structural analysis confirms that substantial alteration of the chemical structure occurs after irradiation. Infrared spectroscopy reveals significant differences in the patterns recorded for the fresh material compared to a sample irradiated for 60 min and 120 min (Fig. S5†). Raman spectroscopy shows that the graphene phase

remains almost entirely intact while the signals from crystalline P25 completely vanished (Fig. 6). Varying the ratio of the two phases seems to trigger the same phenomena, as both  $\text{TiO}_2@\text{GO-05 : 95}$  and  $\text{TiO}_2@\text{GO-95 : 05}$  show the same alterations (Fig. 6). The total destruction of the crystalline phase could also be confirmed based on XRD, where the native peaks of Degussa totally disappeared (Fig. S6†). Indeed, in spite of the straightforwardness of the solvent-free grinding approach, the poor recyclability is the main limitation of the present approach. In addition, powdered forms are not suitable for end use and shaping should be considered.<sup>8</sup>

We therefore preliminarily investigated the possible shaping of the ground formulation into porous beads using renewable biomass-derived chitosan hydrogel. We have previously used chitosan as a mould to grow and shape more sophisticated objects, including metal oxide clusters,<sup>26</sup> metal nanoparticles,<sup>28</sup> clay and graphene sheets,<sup>29</sup> and metal-organic frameworks.<sup>30</sup> We consequently attempted to shape binary  $\text{TiO}_2@\text{GO}$  within singular microspheres. Interestingly, regular porous beads could be obtained using different ratios of chitosan with respect to  $\text{TiO}_2@\text{GO-45 : 55}$ , showing that the powder does not alter the gelation memory of the polysaccharide. As illustrated in the obtained photos, both native  $\text{TiO}_2$  and native GO could also be accommodated in bead-form, and the colour of the microspheres reflects the presence of the embedded phase (Fig. 7). The advantage of these beads is that they can be recovered from the medium using a spatula, without the need for specific filters or tedious workup procedures. Once configured as porous

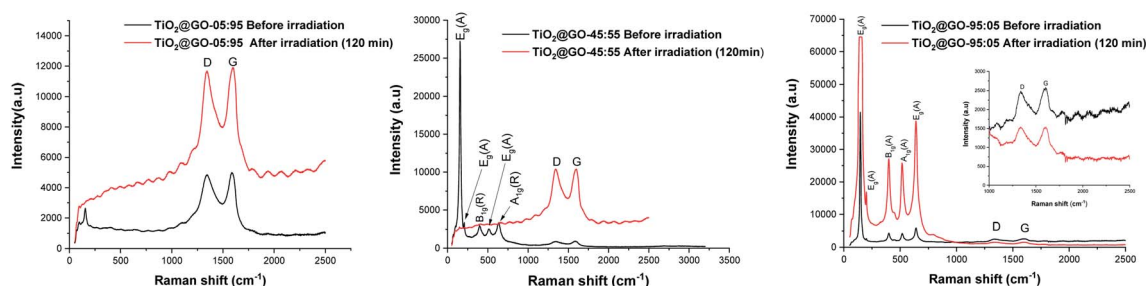


Fig. 6 Raman spectra of the prepared materials before and after irradiation.

beads,  $\text{TiO}_2@\text{GO\_PB}$  (PB refers to porous beads) could be recycled for an extended period of time compared to the non-shaped  $\text{TiO}_2@\text{GO}$  powdered photo-material (Fig. 7). Recent studies have reported the use of hydrogels as photo-reactors,<sup>31</sup> and our results suggest the involvement of the gelling medium to further delay the fast deactivation initially observed for the ground powder. Research in this direction is currently being undertaken to unveil the possible role of the gelling medium during the photooxidation process.

## Experimental section

### General

Fourier-transform infrared (FTIR) spectra were obtained with a PerkinElmer Spectrum 100 FT-IR spectrometer using neat samples (ATR FT-IR). DR-UV spectra were recorded in the 200–800 nm range, with Spectralon as the reference, using a PerkinElmer Lambda 1050 spectrometer equipped with an integrating sphere (Labshare, North Sutton, USA). Nitrogen sorption isotherms were obtained at 77 K with Micromeritics ASAP 2010 apparatus (Micromeritics, Norcross, GA, USA). Prior to measurement, the samples were degassed for 12 h at 100 °C to remove any physisorbed species. X-ray powder diffraction (XRD) patterns were recorded using a D8 Advance Bruker AXS system (Bruker D8 Advance; Bruker Corp, Billerica, MA, USA) using  $\text{CuK}\alpha$  radiation and a step size of 0.02° in the  $2\theta$  range from 0.45 to 87°. Scanning electron microscopy (SEM) images were acquired using a ZEISS ULTRA 55 microscope equipped with an X-ray detector (EDS). Raman spectra were recorded using a 514 nm excitation laser on a Horiba LabRAM HR Evolution spectrometer.

### Materials

Commercially available reagents and solvents were purchased from Acros and Sigma-Aldrich.  $\text{TiO}_2$  powder (average diameter: 30 nm; surface area: 50 m<sup>2</sup> g<sup>-1</sup>, identical to Degussa P25) was supplied by Sigma-Aldrich. Graphene oxide (GO) was obtained *via* the oxidation of graphite flakes using a modified Hummers' method.<sup>32</sup> Chitosan of medium molecular weight with a deacetylation degree of 85% was purchased from Sigma-Aldrich.

### Preparation of mechanochemically ground powder

The different materials were prepared *via* manual grinding using a mortar, for 15 min, starting from a mixture of titanium dioxide and carbon materials, clay, or boron nitride at different ratios. No solvents were used in this process.

### Preparation of $\text{TiO}_2@\text{GO\_us}$

A mixture of 100 mg of  $\text{TiO}_2@\text{GO}$ -45 : 55 in 15 ml of ethanol was kept under sonication for 15 min at a frequency of 45 kHz. Then, the product was recovered after filtration and dried in an oven at 60 °C for 12 h.

### Preparation of $\text{TiO}_2@\text{GO\_reflux}$

100 mg of  $\text{TiO}_2@\text{GO}$ -45 : 55 was added to 15 ml of ethanol in a 50 ml flask. The mixture was maintained under reflux for 1 h. After filtration, the powder was dried in an oven at 60 °C for 12 h.

### Preparation of $\text{TiO}_2@\text{CS\_pyr}$

2.5 ml of titanium isopropoxide was added to a solution of 1 g of chitosan in 150 ml of 1% (v/v) acetic acid solution. The reaction mixture was left under stirring for 36 h at room temperature. The mixture was then dried for 48 h at room temperature. The powder obtained was thermally annealed at 500 °C for 3 h under a  $\text{N}_2$  atmosphere at a heating ramp rate of 5 °C min<sup>-1</sup>.

### Preparation of porous beads

100 mg of chitosan was dissolved in 8 ml of 1% (v/v) acetic acid solution and kept under vigorous stirring for 120 min. Then, GO,  $\text{TiO}_2$ , or  $\text{TiO}_2@\text{GO}$ -45 : 55 was dispersed in 2 ml of 1% (v/v) acetic acid solution and submitted to sonication for 90 min. The suspension was gradually added to the chitosan solution and the resulting mixture was stirred for an additional 90 min. This mixture was dropped into NaOH solution (4 N) using a syringe. The beads were stored in alkaline solution for 2 h before repeated washing with distilled water until the washing water was neutral.

### Photodegradation studies

The photodegradation experiments were carried out *via* combining 80 ml of methylene blue, green malachite, Congo red, or methyl orange solution ( $C_0 = 10^{-3}$  mmol l<sup>-1</sup>) and 50 mg of photocatalyst. The mixture was kept under constant magnetic stirring in the dark during an hour so that the dye adsorption equilibrium was established on the catalyst surface. Then, we exposed the reaction mixture to radiation. Experiments were performed at room temperature. The samples were filtered with a Millipore filter with a pore size of 0.45 μm. The remaining concentration of dye in solution ( $C$ ) was measured using a UV-vis spectrophotometer that had been previously calibrated. The wavelength of maximum absorption ( $\lambda_{\text{max}}$ ) values are 664 nm (methylene blue), 617 nm (green malachite), 500 nm (Congo red), and 464 nm (methyl orange). Between each

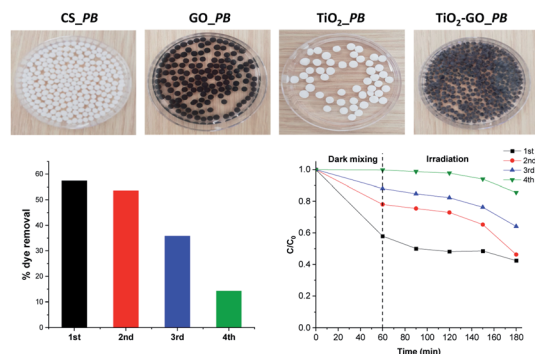


Fig. 7 Configuring the photocatalyst into porous-bead form to improve its recyclability compared to native powder.



catalytic run, the powder was centrifuged, washed with pure water, and dried at 60 °C for 12 h before the next run.

## Conclusions

The simple and fast grinding of P25 Degussa with graphene oxide under solvent-free conditions affords an efficient visible-light-activated photocatalyst, showing a performance contrast with native Degussa, which is devoid of noticeable photoactivity. Broad screening reveals the suitability of graphene oxide for such a purpose, as it outperforms analogues such as P25-graphite, P25-CNT, and P25-AC. This photoactivity enhancement may be rooted in the presence of plentiful oxygenated groups in GO, allowing for more interplay with titanium dioxide Degussa and providing the driving force for sheet exfoliation. Grinding P25 with graphite does not result in spectacular performance, probably because of the difficulty of achieving graphite-sheet exfoliation, making the stacked inter-layer space inaccessible to pollutants. Grinding P25 with clay-based absorbents like layered montmorillonite and nanotubular halloysite failed to achieve the same performance, which further evidences the role of GO as a photosensitizer for titanium dioxide particles. This allows the active region of the heterojunction to be expanded to visible light, where native Degussa is traditionally not active. Our preliminary recycling experiments reveal interesting behavior during the entrapment of the photocatalyst inside of chitosan hydrogels, and this suggests that the performance can be further improved through additional optimization. The timesaving nature and simplicity of the protocol provide a driving force to pursue further efforts to implement this technology on a large scale.

## Conflicts of interest

There are no conflicts to declare.

## Notes and references

- 1 A. Fujishima and K. Honda, *Nature*, 1972, **238**, 37–38.
- 2 C. R. Holkar, A. J. Jadhav, D. V. Pinjari, N. M. Mahamuni and A. B. Pandit, *J. Environ. Manage.*, 2016, **182**, 351–366.
- 3 (a) A. Fujishima, T. N. Rao and D. A. Tryk, *J. Photochem. Photobiol., C*, 2000, **1**, 1–21; (b) X. Chen and S. S. Mao, *Chem. Rev.*, 2007, **107**, 2891–2959; (c) J. Schneider, M. Matsuoka, M. Takeuchi, J. Zhang, Y. Horiuchi, M. Anpo and D. W. Bahnemann, *Chem. Rev.*, 2014, **114**, 9919–9986.
- 4 (a) V. Etacheri, C. Di Valentin, J. Schneider, D. Bahnemann and S. C. Pillai, *J. Photochem. Photobiol., C*, 2015, **25**, 1–29; (b) H. Tong, S. Ouyang, Y. Bi, N. Umezawa, M. Oshikiri and J. Ye, *Adv. Mater.*, 2012, **24**, 229–251.
- 5 (a) V. Subramanian, E. Wolf and P. V. Kamat, *J. Phys. Chem. B*, 2001, **105**, 11439–11446; (b) P. D. Cozzoli, E. Fanizza, R. Comparelli, M. L. Curri, A. Agostiano and D. Laub, *Appl. Catal., B*, 2004, **108**, 9623–9630; (c) M. Besançon, L. Michelin, L. Josien, L. Vidal, K. Assaker, M. Bonne, B. Lebeau and J.-L. Blin, *New J. Chem.*, 2016, **40**, 4386–4397; (d) B. J. Aronson, C. F. Blanford and A. Stein, *Chem. Mater.*, 1997, **9**, 2842–2851; (e) H. Safardoust-Hojaghan and M. Salavati-Niasari, *J. Cleaner Prod.*, 2017, **148**, 31–36; (f) Y. Deng, M. Chen, G. Chen, W. Zou, Y. Zhao, H. Zhang and Q. Zhao, *ACS Omega*, 2021, **6**, 4247–4254; (g) Y. Brahmi, N. Katir, A. Hameau, A. Essoumhi, E. M. Essassi, A.-M. Caminade, M. Bousmina, J.-P. Majoral and A. El Kadib, *Chem. Commun.*, 2011, **47**, 8626–8628; (h) Y. Brahmi, N. Katir, M. Ianchuk, V. Collière, E. M. Essassi, A. Ouali, A.-M. Caminade, M. Bousmina, J. P. Majoral and A. El Kadib, *Nanoscale*, 2013, **5**, 2850–2856; (i) Y. Brahmi, N. Katir, J. A. M. Agullo, A. Primo, M. Bousmina, J. Pierre Majoral, H. Garcia and A. El Kadib, *Dalton Trans.*, 2015, **44**, 15544–15556; (j) N. Katir, Y. Brahmi, J. P. Majoral, M. Bousmina and A. El Kadib, *Chem. Commun.*, 2015, **51**, 17716–17719; (k) N. Katir, N. Marcotte, S. Michlewska, M. Ionov, N. El Brahmi, M. Bousmina, J. P. Majoral, M. Bryszewska and A. El Kadib, *ACS Appl. Nano Mater.*, 2019, **2**, 2979–2990.
- 6 M. Dahl, Y. Liu and Y. Yin, *Chem. Rev.*, 2014, **114**, 9853–9889.
- 7 (a) D. Fattakhova-Rohlfing, A. Zaleska and T. Bein, *Chem. Rev.*, 2014, **114**, 9487–9558; (b) L. Liu and X. Chen, *Chem. Rev.*, 2014, **114**, 9890–9918; (c) H. Chen, C. E. Nanayakkara and V. H. Grassian, *Chem. Rev.*, 2012, **112**, 5919–5948.
- 8 F. Fresno, R. Portela, S. Suárez and J. M. Coronado, *J. Mater. Chem. A*, 2014, **2**, 2863–2884.
- 9 F. Matter and M. Niederberger, *Adv. Sci.*, 2022, **9**, 2105363.
- 10 (a) W. K. Jo, S. H. Shin and E. S. Hwang, *J. Hazard. Mater.*, 2011, **191**, 234–239; (b) P. Bhavani, M. Hussain and Y.-K. Park, *J. Cleaner Prod.*, 2022, **330**, 129899; (c) F. Wang, M. Hao, W. Liu, P. Yan, B. Fang, S. Li, J. Liang, M. Zhu and L. Cui, *Nano Mater. Sci.*, 2021, **3**, 205–212; (d) L. Cui, M. Hao, F. Wang, B. Fang, J. Liang, M. Zhu and X. Xie, *Int. J. Photoenergy*, 2020, **2020**, 8868782.
- 11 (a) Y. Hu, C. Zhou, H. Wang, M. Chen, G. Zeng, Z. Liu, Y. Liu, W. Wang, T. Wu, B. Shao and Q. Liang, *Chem. Eng. J.*, 2021, **414**, 128795; (b) P. Shandilya, A. Guleria and B. Fang, *J. Environ. Chem. Eng.*, 2021, **9**, 106461; (c) G. Liao, C. Li, X. Li and B. Fang, *Cell Rep. Phys. Sci.*, 2021, **2**, 100355; (d) F. Yi, J. Ma, C. Lin, L. Wang, H. Zhang, Y. Qian and K. Zhang, *J. Alloys Compd.*, 2020, **821**, 153557.
- 12 (a) Y. Yao, G. Li, S. Ciston, R. M. Lueptow and K. A. Gray, *Environ. Sci. Technol.*, 2008, **42**, 4952–4957; (b) N. Zhang, M.-Q. Yang, S. Liu, Y. Sun and Y.-J. Xu, *Chem. Rev.*, 2015, **115**, 10307–10377.
- 13 (a) Y. Zhang, Z.-R. Tang, X. Fu and Y.-J. Xu, *ACS Nano*, 2010, **4**, 7303–7314; (b) H. Zhang, X. Lv, Y. Li, Y. Wang and J. Li, *ACS Nano*, 2010, **4**, 380–386; (c) Y. Zhang, Z.-R. Tang, X. Fu and Y.-J. Xu, *ACS Nano*, 2011, **5**, 7426–7435.
- 14 R. Das, C. D. Vecitis, A. Schulze, B. Cao, A. F. Ismail, X. Lu, J. Chen and S. Ramakrishna, *Chem. Soc. Rev.*, 2017, **46**, 6946–7020.
- 15 (a) Y. Liu, D. Zhang, Y. Shang, W. Zang and M. Li, *RSC Adv.*, 2015, **5**, 104785–104791; (b) Z. Qianqian, B. Tang and H. Guoxin, *J. Hazard. Mater.*, 2011, **198**, 78–86.
- 16 (a) S. Frindy, A. Primo, A. e. k. Qaiss, R. Bouhfid, M. Lahcini, H. Garcia, M. Bousmina and A. El Kadib, *Carbohydr. Polym.*, 2016, **146**, 353–361; (b) B. Boumhidi, N. Katir, J. El Haskouri,



- K. Draoui and A. El Kadib, *New J. Chem.*, 2020, **44**, 14136–14144.
- 17 D. Golberg, Y. Bando, Y. Huang, T. Terao, M. Mitome, C. Tang and C. Zhi, *ACS Nano*, 2010, **4**, 2979–2993.
- 18 (a) P. Montes-Navajas, N. G. Asenjo, R. Santamaría, R. Menéndez, A. Corma and H. García, *Langmuir*, 2013, **29**, 13443–13448; (b) L. Chen, C. Batchelor-McAuley, B. Rasche, C. Johnston, N. Hindle and R. G. Compton, *Appl. Mater. Today*, 2020, **18**, 100506.
- 19 H. Ennaji, R. Bouhfid, E. M. Essassi, M. Bousmina and A. El Kadib, *Microporous Mesoporous Mater.*, 2012, **152**, 208–213.
- 20 Y. Li, X. Yuan, L. Jiang, H. Dai, Y. Zhao, X. Guan, J. Bai and H. Wang, *Environ. Sci.: Nano*, 2022, **9**, 841–866.
- 21 (a) H. Xue, Y. Wu, Y. Zou, Y. Shen, G. Liu, Q. Li, D. Yin, L. Wang and J. Ming, *Adv. Funct. Mater.*, 2020, **30**, 1910657; (b) A. Puthirath Balan, S. Radhakrishnan, C. F. Woellner, S. K. Sinha, L. Deng, C. d. I. Reyes, B. M. Rao, M. Paulose, R. Neupane, A. Apte, V. Kochat, R. Vajtai, A. R. Harutyunyan, C.-W. Chu, G. Costin, D. S. Galvao, A. A. Martí, P. A. van Aken, O. K. Varghese, C. S. Tiwary, A. Malie Madom Ramaswamy Iyer and P. M. Ajayan, *Nat. Nanotechnol.*, 2018, **13**, 602–609.
- 22 A. Anouar, N. Katir, A.-S. Mamede, A. Aboulaich, K. Draoui, S. Royer and A. El Kadib, *Mater. Chem. Front.*, 2019, **3**, 242–250.
- 23 F.-E. Zirar, A. Anouar, N. Katir, I. A. Ichou and A. El Kadib, *RSC Adv.*, 2021, **11**, 28116–28125.
- 24 M. Tamtaji, A. Tyagi, C. Y. You, P. R. Galligan, H. Liu, Z. Liu, R. Karimi, Y. Cai, A. P. Roxas, H. Wong and Z. Luo, *ACS Appl. Nano Mater.*, 2021, **4**, 7563–7586.
- 25 N. Hammi, S. Chen, F. Dumeignil, S. Royer and A. El Kadib, *Mater. Today Sustain.*, 2020, **10**, 100053.
- 26 A. El Kadib and M. Bousmina, *Chem.-Eur. J.*, 2012, **18**, 8264–8277.
- 27 S. Frindy, A. El Kadib, M. Lahcini, A. Primo and H. García, *ACS Catal.*, 2016, **6**, 3863–3869.
- 28 (a) A. El Kadib, M. Bousmina and D. Brunel, *J. Nanosci. Nanotechnol.*, 2014, **14**, 308–331; (b) A. Anouar, N. Katir, A. El Kadib, A. Primo and H. García, *Molecules*, 2019, **24**, 3290.
- 29 A. El Kadib, *Chem. Rec.*, 2020, **20**, 753–772.
- 30 N. Hammi, S. Chen, A. Primo, S. Royer, H. Garcia and A. El Kadib, *Green Chem.*, 2022, **24**, 4533–4543.
- 31 R. R. Mansurov, V. S. Zverev and A. P. Safronov, *J. Catal.*, 2022, **406**, 9–18.
- 32 W. S. Hummers and R. E. Offeman, *J. Am. Chem. Soc.*, 1958, **80**, 1339.

